nature energy

ARTICLES

https://doi.org/10.1038/s41560-018-0192-2

Suppression of atomic vacancies via incorporation of isovalent small ions to increase the stability of halide perovskite solar cells in ambient air

Makhsud I. Saidaminov[1,2], Junghwan Kim[1,2], Ankit Jain[1], Rafael Quintero-Bermudez[1], Hairen Tan[1], Guankui Long[1], Furui Tan[1], Andrew Johnston[1], Yicheng Zhao[1], Oleksandr Voznyy[1] and Edward H. Sargent[1]*

The degradation of perovskite solar cells in the presence of trace water and oxygen poses a challenge for their commercial impact given the appreciable permeability of cost-effective encapsulants. Point defects were recently shown to be a major source of decomposition due to their high affinity for water and oxygen molecules. Here, we report that, in single-cation/halide perovskites, local lattice strain facilitates the formation of vacancies and that cation/halide mixing suppresses their formation via strain relaxation. We then show that judiciously selected dopants can maximize the formation energy of defects responsible for degradation. Cd-containing cells show an order of magnitude enhanced unencapsulated stability compared to state-of-art mixed perovskite solar cells, for both shelf storage and maximum power point operation in ambient air at a relative humidity of 50%. We conclude by testing the generalizability of the defect engineering concept, demonstrating both vacancy-formation suppressors (such as Zn) and promoters (such as Hg).

The power conversion efficiency (PCE) of $MAPbI_3$-based solar cells ($MA = CH_3NH_3^+$) has improved rapidly in the past five years[1–7]. However, instability in $MAPbI_3$ limits this active material's applicability in perovskite solar cell (PSC) technology[8]. Notable progress toward increasing the stability of PSCs was recently made via the engineering of interfaces[9–11] and of carrier selective layers[12,13]. Developing even more stable perovskite active layers is now a topic that requires further effort. The incorporation of low-dimensional structures is an attractive approach to improve the stability of perovskites[14,15], but, at present, compromises PCE.

Replacing MA with FA ($HC(NH_2)_2^+$) has been found to produce perovskites relatively stable against decomposition at high temperatures[16]; however, at room temperature, $FAPbI_3$ is structurally unstable owing to the large size of the FA cation: it spontaneously transforms into a yellow, non-functional phase. The structural instability of $FAPbI_3$ was recently addressed by engineering the Goldschmidt tolerance factor in perovskites via the partial substitution of MA and/or Cs for FA, and Br for I (refs [17–23]). Cation/anion mixed PSCs were shown to operate stably at maximum power point (MPP) conditions under continuous illumination and nitrogen flow for hundreds of hours[24,25].

The structural stability of mixed perovskites can be understood in terms of steric effects[26,27] and energy gain from entropy of mixing[28–31]; nevertheless, the mechanisms that prevent the decomposition of these perovskites remain incompletely understood. Understanding the factors governing stability against decomposition will enable fabrication of PSCs that are more tolerant to ambient air. The need for air-tolerant solar cells arises from the high water vapour and oxygen transmission rates of cost-effective photovoltaic encapsulation materials, which until now have been insufficient for the protection of PSCs[32]; in contrast, the best alternative atmospheric barriers work well with perovskites, but add cost[8,33] (Supplementary Table 1). The development of air-ambient-tolerant perovskite active layers will ensure that practical encapsulation technologies can be applied.

Here, we report that, in single-cation/halide $FAPbI_3$, local lattice strain induces the formation of point defects, recently shown to be a major source of degradation in PSCs. We then show that incorporation of Cs/MA/Br ions in the state-of-art CsMAFA perovskite ($Cs_{0.05}MA_{0.15}FA_{0.8}PbI_{2.55}Br_{0.45}$)[21,25] increases the formation energy of vacancies, consistent with this material's impressive initial performance. However, we also show that such defects, even if rare, have a high affinity for water and oxygen molecules; and that even a small density of these defects is highly detrimental. Further increasing the Cs/Br content blueshifts the bandgap, which works against the PSC power conversion efficiency. We therefore sought new strategies to suppress vacancy formation, and report herein the incorporation of judiciously selected B-site dopants into the lattice of mixed perovskite crystals. We incorporate cadmium (Cd) into a mixed perovskite lattice, releasing the remaining lattice strain and further increasing the energetic cost associated with the formation of vacancies. The resultant unencapsulated PSCs show significantly extended stability: they maintain >90% of their initial PCE after 30 days of storage in ambient air at a relative humidity of 50%. They also show an order of magnitude longer operating MPP lifetime under these same ambient air and relative humidity conditions compared to state-of-art CsMAFA perovskite solar cells.

Properties of CsMAFA single crystals

We sought first to understand why mixed CsMAFA perovskites perform better in solar cell active layers than $MAPbI_3$ or $FAPbI_3$ (refs [21,25]). To exclude the effects of grain boundaries that are abundant in thin films, we first studied the properties of CsMAFA single crystals. The powder X-ray diffraction patterns of ground crystals

[1]Department of Electrical and Computer Engineering, University of Toronto, Toronto, Ontario, Canada. [2]These authors contributed equally to this work: Makhsud I. Saidaminov, Junghwan Kim. *e-mail: ted.sargent@utoronto.ca

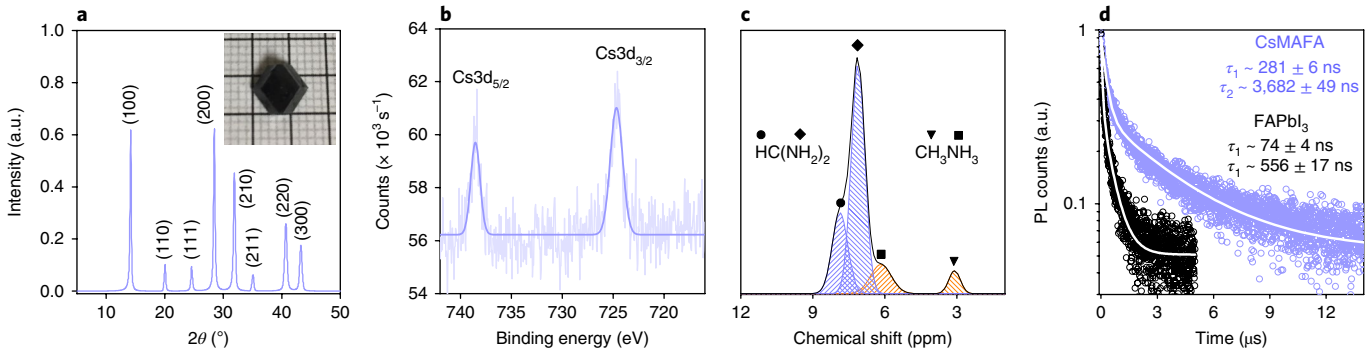

Fig. 1 | Characterization of CsMAFA single crystals. a, X-ray diffraction of a ground crystal, confirming the single phase. The inset shows a ~7 mm × 7 mm × 3 mm CsMAFA crystal. The peaks were indexed with a cubic crystallographic phase and $a = 6.25$ Å, slightly smaller than that of $FAPbI_3$ ($a = 6.36$ Å)[26], indicating the successful incorporation of Cs and Br within the crystal lattice. **b**, XPS of Cs 3*d* levels in a cleaved CsMAFA crystal. The solid curve represents a Gaussian fit. **c**, Solid-state ^{1}H NMR revealing the presence of both FA and MA cations. The spectrum was deconvolved using Gaussian fitting. **d**, PL lifetime traces of CsMAFA and $FAPbI_3$ single crystals fitted with biexponential decay.

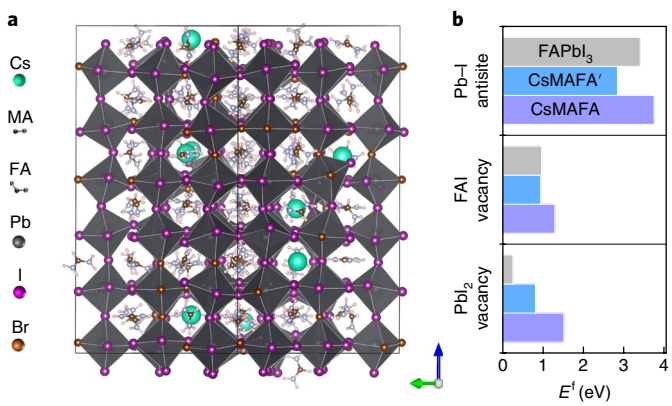

Fig. 2 | Formation energies of antisites and Schottky vacancies. a, The supercell used in DFT calculations. **b**, Formation energies of antisites and Schottky vacancies in $FAPbI_3$ and CsMAFA perovskites. Compositions simulated using DFT: $FA_{108}Pb_{108}I_{324}$ ($FAPbI_3$); $Cs_2MA_{12}FA_{94}Pb_{108}Br_{55}I_{269}$ (CsMAFA′); $Cs_8MA_{12}FA_{88}Pb_{108}Br_{55}I_{269}$ (CsMAFA).

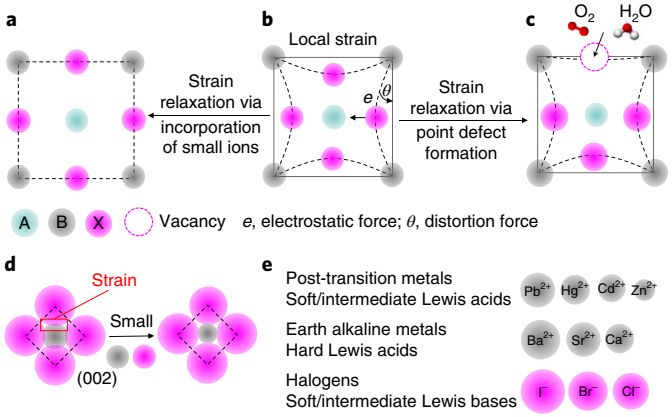

Fig. 3 | Mechanisms of lattice relaxation. a–c, Schematic illustrating the local strain (**b**), which is reduced either by the formation of point defects (**c**) or by the incorporation of small ions (**a**). The distortion angle ($\theta = 180°$ – angle(B–X–B′)) decreases via strain relaxation. **d**, Schematic demonstrating the strain in the (002) plane, which is reduced by incorporation of small B/X-site ions. **e**, B/X isovalent candidates for incorporation.

showed a single cubic phase (Fig. 1a). We found an elemental composition in the crystal similar to that in the feed solution (Fig. 1b,c, Supplementary Fig. 1 and Supplementary Table 2). Photoluminescence (PL) lifetime measurements of CsMAFA single crystals (Fig. 1d) revealed remarkably long carrier lifetimes (~0.3 and ~3.7 μs of the fast and slow components, respectively), six times greater than those of identically grown black $FAPbI_3$ single crystals (Fig. 1d), pointing to substantially reduced trap states in CsMAFA. This finding agrees with the improved performance of mixed perovskites relative to single-cation/halide perovskites[21].

Lattice strain relaxation mechanisms in perovskites

To gain insight into the origins of improved stability of CsMAFA[21,25], we calculated the formation energies of $FAPbI_3$ and CsMAFA as well as antisites and Schottky vacancies (stoichiometric amount of anion and cation vacancies) for large supercells (Fig. 2a) using density functional theory (DFT, see Methods and Supplementary Data 1). We did not find a notable difference in the formation energies of the compounds (Supplementary Table 3). Similarly, the formation of Pb–I antisites, the most probable deep electronic traps[34], is equally unlikely given their high formation energies (Fig. 2b).

In contrast, we found a significant difference in the formation energies associated with lead iodide vacancies (Fig. 2b). In $FAPbI_3$, this energy is remarkably low (~0.25 eV), corresponding to an equilibrium PbI_2 vacancy density of $\sim 3 \times 10^{17}$ cm^{-3} (Supplementary Table 4). When FA and I are partially replaced with Cs/MA and Br, respectively, the PbI_2 vacancy formation energy is increased more than threefold, corresponding to reducing the vacancy concentration by an estimated factor of 10^9.

We account for this through the pathways of lattice strain relaxation depicted in Fig. 3a–c. Strain originates from the ionic size mismatch between the A cation and the lead halide cage size resulting in cage distortions and BX_6 octahedra tilting (Fig. 3b). The strain in $FAPbI_3$ is reduced by point defect formation in $FAPbI_3$ (Fig. 3c and Supplementary Fig. 2); this mechanism of lattice relaxation via vacancy formation has been observed in oxide perovskites[35].

To elucidate further the role of lattice strain relaxation on the formation of vacancies, we expanded the cage by 2% (this decreases the Pb–I–Pb distortion angles, a result also achieved by the incorporation of small ions; Supplementary Fig. 3) in $FAPbI_3$ and found that the PbI_2 vacancy formation energy increases by 0.55 eV. This suggests that the incorporation of small ions prevents the formation of defects by opening a new lattice strain relaxation pathway in CsMAFA (Fig. 3a), which is otherwise reached by vacancy formation in single-cation/anion perovskites.

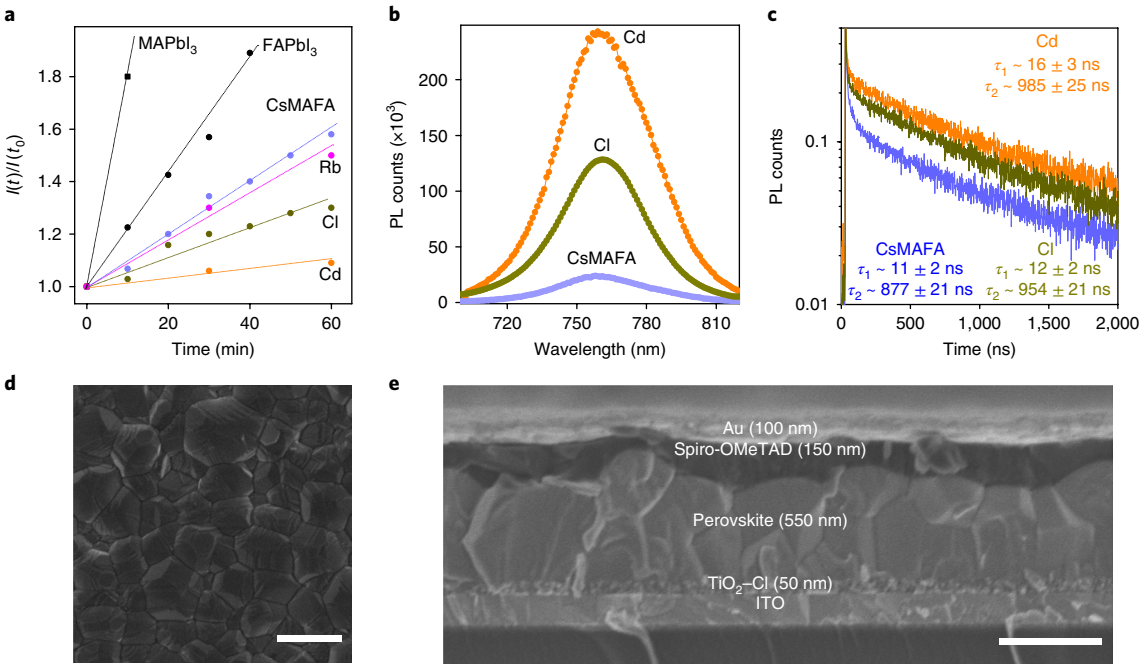

Fig. 4 | Characterization of CsMAFA perovskite films with and without dopants. a, Normalized PL intensity of hydroethidine aliquots in which films were aged under light and oxygen blow at 610 nm, representing the yield of superoxide generation. The dotted lines are guides for the eye. **b**, Time-integrated PL spectra. **c**, Time-dependent PL traces fitted with a biexponential. **d**,**e**, Surface (**d**) and cross-section (**e**) scanning electron micrographs of Cd-containing PSCs. Scale bars, 500 nm. ITO, indium tin oxide.

The role of vacancies in degradation of perovskites

Though perovskite vacancies are shallow electronic traps[34], they hold the potential to cause the formation of deep traps if they react with the ambient environment. The absorption of water and oxygen molecules at vacancy sites is significantly more favourable than at pristine surfaces[36,37], accelerating perovskite degradation via the vacancy-assisted decomposition mechanism. We explored experimentally the results of our computational studies by measuring the rate of superoxide generation, an indicator of the density of vacancies in perovskites, using a hydroethidine fluorescent probe[37,38]: we found the superoxide yield to be significantly reduced in CsMAFA films compared to $MAPbI_3$ and $FAPbI_3$ films (Fig. 4a and Supplementary Fig. 4).

The vacancy-assisted mechanism of perovskite decomposition suggests a means to increase further the stability of perovskites in ambient air. Our concept is to relax the remaining lattice strain on B/X sites (Fig. 3d) to maximize further the formation energy of the most abundant defect without introducing electronic traps. We therefore chose isovalent dopants as candidates (Fig. 3e and Supplementary Table 5), noting that heterovalent dopants may introduce more defects[39].

Suppression of vacancies via incorporation of Cl

We start with incorporation of Cl^- as a promising test case for this purpose, as it is isoelectronic with I^- and may further decrease the lattice strain due to its small ionic radius. Previous reports found that Cl blended into $MAPbI_3$ solution enhances the carrier transport in the ultimate perovskite film[40,41]. Recent studies established that there is no Cl in the final crystal lattice[42] and that Cl may reside only at the interface[43–46]; thus, its role was attributed to the morphological evolution of $MAPbI_3$ (refs [47–49]). Here, we explore instead Cl incorporation within the CsMAFA lattice with the goal of preventing the formation of vacancies, identifying a new role for Cl that enables air-ambient-tolerant perovskites.

We first carried out DFT calculations to investigate the role of Cl in relaxing the lattice strain and reducing the vacancy density. We found that when I was partially replaced by Cl, the Pb–X bond lengths decreased, as did the Pb–X–Pb distortion angles[50] (Supplementary Fig. 3), and the I vacancy formation is suppressed by ≥ 0.3 eV (Supplementary Fig. 5). The formation of a charged defect favours the formation of a counter-charged defect in perovskites, which subsequently form charge-neutral Schottky defect pairs (Supplementary Fig. 6)[51].

We then fabricated Cl-containing CsMAFA films using $PbCl_2$ as a Cl source mixed in solution (see Methods). The reduced superoxide generation indicates that Cl suppresses the density of defects (Fig. 4a). In particular, in ambient air with a relative humidity of 50%, CsMAFA films degraded within less than 7 days, while the films with Cl remained dark (Supplementary Fig. 7). We also observed improved stability of Cl-containing CsMAFA films over control CsMAFA films when subjected to thermal stress (85 °C) in ambient air (Supplementary Fig. 8).

To ascertain whether Cl is incorporated within the crystal structure, we grew single crystals in the presence of Cl, and performed X-ray photoemission spectroscopy (XPS) of the cleaved interior of the crystal. The results showed the successful incorporation of Cl within CsMAFA perovskite (Supplementary Fig. 9). Thus, in contrast with $MAPbI_3$, CsMAFA is able to host Cl; we explain this by noting the ~1/6 occupancy of the CsMAFA halide site with Br (Br-based perovskites can form solid solutions with both I and Cl)[52] and the presence of Cs ($CsPbI_3$ can host Cl at levels near the solubility of Cl in $CsPbI_3$)[53].

Suppression of vacancies via incorporation of Cd

The mechanism of lattice strain relaxation via the incorporation of small monovalent halogen anions (Cl) suppressed the formation of vacancies and, consequently, enhanced the stability. However, the incorporation of additional Cl will increase the bandgap, undesirable for solar cells (Supplementary Fig. 10). We therefore expanded our concept of lattice strain relaxation to include B-site dopants (Fig. 3c). We chose Cd, which is isovalent to Pb but has a smaller ionic radius (Supplementary Table 5), the prerequisites for further strain relaxation without introducing traps.

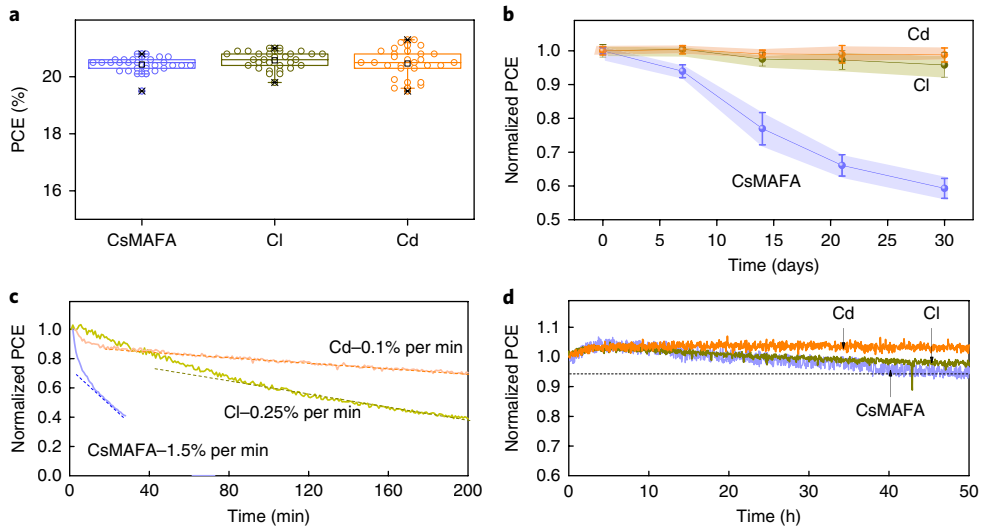

Fig. 5 | Performance of CsMAFA PSCs with and without dopants. **a**, PCE statistics of 30 fresh PSCs for each composition, fabricated in four identical runs. The boxes indicate the 25th and 75th percentiles. The whiskers indicate the 5th and 95th percentiles. The median and mean are represented by the line dividing the boxes and the open square symbols, respectively. The cross symbols represent the maximum and minimum values. **b**, Evolution of PCEs of solar cells on ageing in ambient air (relative humidity of 50%) for six devices. The shaded regions connect the error bars, which are defined as the standard deviation for six devices. **c**,**d**, Operation of unencapsulated PSCs under MPP conditions with a 420 nm cutoff UV filter in ambient air (**c**) and in a nitrogen atmosphere (**d**).

DFT calculations showed that Cd incorporation indeed relaxes the lattice strain (Supplementary Fig. 3) and suppresses the formation energy of I vacancy by ≥0.5 eV (Supplementary Fig. 5); that is, to an appreciably greater extent than does Cl incorporation.

We measured a significantly further-reduced rate of superoxide generation in the films with Cd (Fig. 4a). We also observed successful incorporation of Cd within the perovskite crystal lattice (Supplementary Fig. 9), in agreement with previous findings[54]. We note that Rb-containing CsMAFA showed no reduction in the rate of superoxide generation (Fig. 4a). This may arise due to a failure of Rb to incorporate within the crystal lattice[55].

Incorporation of Cl and Cd increased the PL intensity of films fivefold and tenfold, respectively (Fig. 4b). PL lifetime measurements revealed that Cl and Cd incorporation decreases twofold the integrated contribution of the short recombination term and notably increases the integrated counts of the long recombination term (Fig. 4c and Supplementary Fig. 11). Identical X-ray diffraction patterns and scanning electron micrographs (Fig. 4d,e and Supplementary Fig. 12) indicate that the lattice parameters and morphology are preserved at the Cl and Cd concentrations used herein.

PSC performance and stability

With the goal of improving the stability in Cl and Cd films, we sought to quantify the impact of Cl and Cd integration on PSC devices. We fabricated PSCs in planar architecture following the recently reported CsMAFA PSCs on Cl-capped TiO_2 with 20.1% certified PCE[25] that also served as a control device.

Freshly fabricated CsMAFA, Cl- and Cd-PSCs showed similar average PCEs of ~20.5%, open-circuit voltages (V_{oc}) of 1.16 V, fill factors of ~80% and short-circuit current densities (J_{sc}) of ~22 mA cm^{-2} (Fig. 5a and Supplementary Fig. 13); the J_{sc} agrees with the external quantum yield (EQE) measurements (Supplementary Fig. 14).

The devices showed a large difference in stability when stored in ambient air at a relative humidity of 50% (Fig. 5b). Unencapsulated Cl- and Cd-PSCs retained >95% of their initial PCE after storage in the dark in ambient air for 30 days. In contrast, CsMAFA PSCs retained only 60% of their initial PCE and exhibited bleaching (Supplementary Fig. 7).

We also investigated the photostability of unencapsulated PSCs under MPP operation and continuous illumination in ambient air. CsMAFA cells showed a rapid loss of PCE with relative −1.5% min^{-1} of linear slope[56], while Cl and Cd cells extended the lifetime by a factor of 6 and 15, respectively (Fig. 5c and Supplementary Fig. 15). The extended stability of Cd-containing PSCs agrees with our computational results as well as our experimental measurements of the superoxide generation rate. In a nitrogen atmosphere, all PSCs retained >90% of their initial PCE after continuous MPP for tens of hours (Fig. 5d), indicating that the moisture and oxygen in air play a vital role in their decomposition.

Defects in perovskites assist segregation of halides under illumination, leading to hysteresis[57]. In agreement with the finding herein, we found large hysteresis in $MAPbI_3$- and $FAPbI_3$-based PSCs, whereas hysteresis for mixed PSCs was negligible (Supplementary Table 6). The CsMAFA treatment with MACl and vinyl benzyl chloride also enhanced PL peaks as a result of surface passivation (Supplementary Fig. 16); however, devices showed poor performance and large hysteresis (Supplementary Table 6 and Supplementary Fig. 17). We attribute this to off-stoichiometric surface composition after treatment. Engineering of defects in the bulk and at the surface is likely to be crucial to the combination of performance and stability in PSCs.

In light of the proposed vacancy engineering mechanisms, we also explored the effect of other divalent dopants such as hard Lewis acids (Group 2: Ba, Ca and Sr) and soft/intermediate Lewis acids (Group 12: Hg and Zn) on the performance of PSCs (Supplementary Fig. 18). Hard Lewis acids showed a notably decreased time-zero PCE, probably due to a lack of incorporation and formation of traps; this agrees with the Pearson hard and soft acid and base theory whereby soft I^- base forms a stronger bond with soft acid Pb^{2+}. Zn-doped PSCs showed promising stability; however, the time-zero PCE of devices was slightly decreased, a subject for future studies. Hg-containing PSCs exhibited an opposite trend: comparable initial PCE, but substantial degradation within a few days, probably due to the formation of heterovalent Hg^+ that introduces more vacancies[39]. These findings agree with our DFT findings (Supplementary Fig. 5) that Zn suppresses the formation of vacancies, while Hg is a vacancy-formation promoter.

Conclusions

As the standard photovoltaic encapsulation materials transmit water and oxygen at a rate sufficient for complete degradation of perovskites within a few days (Supplementary Table 1)[32], it is desirable to realize PSCs that exhibit enhanced operating stability in ambient air to ensure that realistic encapsulation technologies can be used. Mixed CsMAFA perovskite is less prone to form vacancies compared to single-cation/anion perovskites, and therefore is more stable against decomposition. Suppressing atomic vacancies via incorporation of Cd and Cl within the CsMAFA lattice further enhances the ambient-air MPP operational stability of state-of-art PSCs by an order of magnitude. This in turn significantly relaxes the requirements for encapsulation materials and their processing conditions. The proposed degradation mechanism and vacancy engineering strategy via lattice strain relaxation open a new avenue to enable continued progress toward PSCs with a 25-year operating lifetime with practical encapsulants.

Methods

Chemicals. Anhydrous lead iodide (PbI_2), lead bromide ($PbBr_2$), lead chloride ($PbCl_2$), cadmium iodide (CdI_2), hydroethidine, 4-vinylbenzyl chloride (VBCl), gamma-butyrolactone (GBL), anhydrous dimethylsulfoxide (DMSO), anhydrous dimethylformamide (DMF), anhydrous isopropyl alcohol (IPA), chlorobenzene (CB), anhydrous toluene, methylamine (33 wt% in absolute ethanol), hydrochloride acid (37 wt% in water) and hydroethidine were purchased from Sigma Aldrich. Formamidinium iodide (FAI) and methylammonium bromide (MABr) were purchased from Dyesol. All salts and solvents were used as received without any further purification.

MACl was synthesized by reacting methylamine and hydrochloride acid with the molar ratio of 1.2:1 in an ice bath for 2 h. The reaction mixture was dried at 50 °C for 2 h under vacuum. Then the collected powder was purified twice by recrystallization from ethanol solution with diethyl ether. Finally, the white powder was dried under vacuum at 60 °C overnight.

Crystal growth. Crystals were synthesized using inverse temperature crystallization[58–62]. To grow $Cs_{0.05}MA_{0.15}FA_{0.8}PbI_{2.55}Br_{0.45}$ crystals, 52 mg CsI (0.2 mmol), 67 mg MABr (0.6 mmol), 550 mg FAI (3.2 mmol), 220 mg $PbBr_2$ (0.6 mmol) and 1.54 g PbI_2 (3.4 mmol) were dissolved in 4 ml GBL and placed in an oil bath at 60 °C. Then the temperature was gradually increased at a rate of 10 K h^{-1}, until 110 °C. The solution was kept at this temperature for 4 h, and then the crystals were collected.

Preparation of solutions for solar cell fabrication. The Cl-capped TiO_2 was prepared following the procedure reported elsewhere[25]. For the CsMAFA, CsI, MABr, FAI, PbI_2 and $PbBr_2$ were dissolved in a DMSO/DMF (1:4) mixture solution in the following molar ratios: $PbI_2/PbBr_2 = 0.85:0.15$, CsI/FAI/MABr = 0.05:0.80:0.15 and $(FAI + MABr + CsI)/(PbI_2 + PbBr_2) = 1:1$ to get the final concentration of 1.4 M.

For CsMAFA-Cl, 28 mg $PbCl_2$ was dissolved in 1 ml of CsMAFA solution to get 5% Cl-containing solution. Lower concentrations of Cl-containing solutions were prepared by mixing the desired ratio of CsMAFA and 5%-Cl-containing solutions.

For CsMAFA-Cd, 10 mg CdI_2 was dissolved in 1 ml of CsMAFA solution to get a Cd-containing solution.

One square metre of such a PSC module will have less heavy metals (Pb and Cd) than a 1-cm-thick slice of natural soil of the same area[63].

Spiro solution was prepared in chlorobenzene with 65 mg ml^{-1} Spiro-OMeTAD and 20 µl ml^{-1} *tert*-butylpyridine, as well as 70 µl ml^{-1} bis(trifluoromethane) sulfonimide lithium salt (170 mg ml^{-1} in acetonitrile).

PSC fabrication. Pre-patterned indium tin oxide (ITO, TFD Devices)-coated glass was cleaned by acetone and isopropanol. The Cl-capped TiO_2 was then spin-coated on ITO substrate, and annealed on a hot plate at 150 °C for 30 min in ambient air. The perovskite films were deposited onto the TiO_2 substrates with a two-step spin-coating procedure. The first step was 1,000 r.p.m. for 10 s with an acceleration of 200 r.p.m. s^{-1}. The second step was 6,000 r.p.m. for 20 s with a ramp-up of 2,000 r.p.m. s^{-1}. Chlorobenzene (150 µl) was dropped on the spinning substrate during the second spin-coating step at 5 s before the end of the procedure. The substrate was then immediately transferred onto a hotplate and heated at 100 °C for 30 min. The spiro was deposited following a dynamic spin-coating method[12]: during spin-coating at 4,000 r.p.m. for 30 s, 70 µl of Spiro solution was dropped onto the substrate 20 s before the end. Finally, a 100 nm Au contact was deposited by electron-beam evaporation.

Surface-treated films were obtained by spin-coating MACl/IPA (1 mg ml^{-1}) or VBCl/IPA (1 mg ml^{-1}) on CsMAFA films at 4,000 r.p.m. for 35 s, and annealing at 100 °C for 10 min.

$FAPbI_3$ films were deposited from a 1.4 M solution of $FAPbI_3$ in DMSO/DMF (1:4) at 6,000 r.p.m. for 20 s (CB was dropped onto the substrate 5 s before the end), followed by 20 min annealing at 150 °C.

$MAPbI_3$ films were deposited from 1.4 M solution of $MAPbI_3$ in DMSO/DMF (1:1) at 5,000 r.p.m. for 60 s (CB was dropped onto the substrate 5 s before the end), followed by 20 min of annealing at 100 °C (ref. [64]).

Solar cell characterization. The *J*–*V* characteristics were measured using a Keithley 2400 sourcemeter under the illumination of a solar simulator (Newport, Class A) at a light intensity of 100 mW cm^{-2}. Unless otherwise stated, the *J*–*V* curves were measured in a nitrogen atmosphere with a scanning rate of 50 mV s^{-1} (voltage step of 10 mV and delay time of 200 ms). Note that a faster scan rate increases hysteresis (Supplementary Fig. 19). The steady-state PCE, PCE(*t*), was measured by setting the bias voltage to the V_{MPP} and then tracing the current density. The V_{MPP} was determined from the *J*–*V* curve. The active area was determined by the aperture shade mask (0.049 cm^2) placed in front of the solar cell to avoid overestimation of the photocurrent density. EQE measurements were performed using ORIEL QuantX 300. The photodiode used for the calibration of EQE measurements has been calibrated by Newport. The dark long-term stability assessment of solar cells was carried out by repeating the *J*–*V* characterizations over various times. The devices without encapsulation were stored in a cabinet with ambient air with a relative humidity of 50%. The stability test at continuous MPP operation under 1 sun, AM 1.5 G illumination was carried out in nitrogen and ambient air by fixing the voltage at V_{MPP} and then tracking the current output. A 420-nm cutoff UV filter was applied in front of the solar cells during the MPP tracking tests.

Other characterizations. High-resolution scanning electron micrographs were obtained using the Hitachi S-5200 microscope with an accelerating voltage of 1 kV. X-ray diffraction patterns were collected using a Rigaku MiniFlex 600 diffractometer equipped with a NaI scintillation counter and using monochromatized copper Kα radiation ($\lambda = 1.5406$ Å). XPS analysis was carried out using the Thermo Scientific K-Alpha XPS system, with a 300 µm spot size, 75 eV pass energy and energy steps of 0.05 eV. Optical absorption measurements were carried out in a Lambda 950 UV/Vis spectrophotometer. PL was measured using a Horiba Fluorolog time-correlated single-photon-counting system with photomultiplier tube detectors. The excitation source is a laser diode at a wavelength of 504 nm. Superoxide generation was measured following the method reported elsewhere[38].

DFT simulations. The DFT calculations were performed using a Perdew–Burkew–Ernzerhof generalized gradient exchange-correlation functional[65]. All calculations were performed using a plane-wave basis set, using projected augmented wave pseudopotentials as implemented in the quantum chemistry code VASP[66]. The plane-wave kinetic energy cutoff was fixed at 400 eV and the van der Waals interactions were modelled using the DFT-D2 scheme of Grimme[67]. The computational cell consisting of 108 $APbX_3$ units was employed in all calculations. The Brillouin zone was sampled using a gamma-only wavevector grid and an electronic convergence criterion of 10^{-7} eV per formula unit was used. The computational cells were initially obtained using periodic repetition of unit cells and were then heated to 300 K using NVT molecular dynamics simulations to obtain random orientations of organic molecules as would be present in real materials. After 3 ps simulations using a 1 fs time step, the structures were cooled down to 0 K and were relaxed using a conjugate gradient algorithm to within 10^{-5} eV per formula unit. Representative VASP input files are provided in Supplementary Data 1.

Mixed CsMAFA perovskites were obtained by randomly replacing the desired number of FA with Cs/MA; and of I with Br. We calculated the formation energies of single-cation/anion and mixed perovskites as:

$$E^f_{FAPbI_3} = \frac{1}{108}(E_{FAPbI_3} - 108E_{FAI} - 108E_{PbI_2})$$

$$E^f_{Cs_2MA_{12}FA_{94}Pb_{108}Br_{55}I_{269}} = \frac{1}{108}(E_{Cs_2MA_{12}FA_{94}Pb_{108}Br_{55}I_{269}} - 2E_{CsI} - 12E_{MABr} - 94E_{FAI} - 21.5E_{PbBr_2} - 86.5E_{PbI_2})$$

$$E^f_{Cs_8MA_{12}FA_{88}Pb_{108}Br_{55}I_{269}} = \frac{1}{108}(E_{Cs_8MA_{12}FA_{88}Pb_{108}Br_{55}I_{269}} - 8E_{CsI} - 12E_{MABr} - 88E_{FAI} - 21.5E_{PbBr_2} - 86.5E_{PbI_2})$$

where E^f_* are desired formation energies and E_* is the DFT-obtained energy of compound *.

The antisite and vacancy defects were created by randomly replacing/removing desired species from 108 formula-unit computational cells. The defect formation energies of charged-neutral defects were obtained as:

$$E^f_a = E_{defect} - E_{perfect}$$

$$E_v^f = E_{defect} + E_* - E_{perfect}$$

where E_a^f, E_v^f are antisite and vacancy defect formation energies, E_{defect}, $E_{perfect}$ are DFT-calculated energies of defected and perfect structures, and E_* is the DFT-calculated energy of removed bulk molecules (FAI or PbI_2).

Reporting Summary. Further information on experimental design is available in the Nature Research Reporting Summary linked to this article.

Data availability. The authors declare that the main data supporting the findings of this study are available within the article and its Supplementary Information. Extra data are available from the authors upon request.

Received: 1 February 2018; Accepted: 30 May 2018;
Published online: 16 July 2018

References

1. Kojima, A., Teshima, K., Shirai, Y. & Miyasaka, T. Organometal halide perovskites as visible-light sensitizers for photovoltaic cells. *J. Am. Chem. Soc.* **131**, 6050–6051 (2009).
2. Im, J.-H., Lee, C.-R., Lee, J.-W., Park, S.-W. & Park, N.-G. 6.5% efficient perovskite quantum-dot-sensitized solar cell. *Nanoscale* **3**, 4088 (2011).
3. Kim, H.-S. et al. Lead iodide perovskite sensitized all-solid-state submicron thin film mesoscopic solar cell with efficiency exceeding 9%. *Sci. Rep.* **2**, 591 (2012).
4. Burschka, J. et al. Sequential deposition as a route to high-performance perovskite-sensitized solar cells. *Nature* **499**, 316–320 (2013).
5. Hao, F., Stoumpos, C. C., Liu, Z., Chang, R. P. H. & Kanatzidis, M. G. Controllable perovskite crystallization at a gas–solid interface for hole conductor-free solar cells with steady power conversion efficiency over 10%. *J. Am. Chem. Soc.* **136**, 16411–16419 (2014).
6. Im, J.-H., Jang, I.-H., Pellet, N., Grätzel, M. & Park, N.-G. Growth of $CH_3NH_3PbI_3$ cuboids with controlled size for high-efficiency perovskite solar cells. *Nat. Nanotech.* **9**, 927–932 (2014).
7. Stranks, S. D. & Snaith, H. J. Metal-halide perovskites for photovoltaic and light-emitting devices. *Nat. Nanotech.* **10**, 391–402 (2015).
8. Yang, Y. & You, J. Make perovskite solar cells stable. *Nature* **544**, 155–156 (2017).
9. Christians, J. A. et al. Tailored interfaces of unencapsulated perovskite solar cells for > 1,000 hour operational stability. *Nat. Energy* **3**, 68–74 (2018).
10. Hou, Y. et al. A generic interface to reduce the efficiency-stability-cost gap of perovskite solar cells. *Science* **358**, 1192–1197 (2017).
11. Zhao, P., Kim, B. J. & Jung, H. S. Passivation in perovskite solar cells: A review. *Mater. Today Energy* **7**, 267–286 (2018).
12. Arora, N. et al. Perovskite solar cells with CuSCN hole extraction layers yield stabilized efficiencies greater than 20%. *Science* **358**, 768–771 (2017).
13. You, J. et al. Improved air stability of perovskite solar cells via solution-processed metal oxide transport layers. *Nat. Nanotech.* **11**, 75–81 (2015).
14. Wang, Z. et al. Efficient ambient-air-stable solar cells with 2D–3D heterostructured butylammonium-caesium-formamidinium lead halide perovskites. *Nat. Energy* **2**, 17135 (2017).
15. Tsai, H. et al. High-efficiency two-dimensional Ruddlesden–Popper perovskite solar cells. *Nature* **536**, 312–316 (2016).
16. Eperon, G. E. et al. Formamidinium lead trihalide: a broadly tunable perovskite for efficient planar heterojunction solar cells. *Energy Environ. Sci.* **7**, 982 (2014).
17. Lee, J.-W. et al. Formamidinium and cesium hybridization for photo- and moisture-stable perovskite solar cell. *Adv. Energy Mater.* **5**, 1501310 (2015).
18. Li, Z. et al. Stabilizing perovskite structures by tuning tolerance factor: formation of formamidinium and cesium lead iodide solid-state alloys. *Chem. Mater.* **28**, 284–292 (2016).
19. McMeekin, D. P. et al. A mixed-cation lead mixed-halide perovskite absorber for tandem solar cells. *Science* **351**, 151–155 (2016).
20. Jeon, N. J. et al. Compositional engineering of perovskite materials for high-performance solar cells. *Nature* **517**, 476–480 (2015).
21. Saliba, M. et al. Cesium-containing triple cation perovskite solar cells: improved stability, reproducibility and high efficiency. *Energy Environ. Sci.* **9**, 1989–1997 (2016).
22. Bush, K. A. et al. 23.6%-efficient monolithic perovskite/silicon tandem solar cells with improved stability. *Nat. Energy* **2**, 17009 (2017).
23. Amat, A. et al. Cation-induced band-gap tuning in organohalide perovskites: interplay of spin–orbit coupling and octahedra tilting. *Nano Lett.* **14**, 3608–3616 (2014).
24. Saliba, M. et al. Incorporation of rubidium cations into perovskite solar cells improves photovoltaic performance. *Science* **354**, 206–209 (2016).
25. Tan, H. et al. Efficient and stable solution-processed planar perovskite solar cells via contact passivation. *Science* **355**, 722–726 (2017).
26. Xie, L. et al. Understanding the cubic phase stabilization and crystallization kinetics in mixed cations and halides perovskite single crystals. *J. Am. Chem. Soc.* **139**, 3320–3323 (2017).
27. Zheng, X. et al. Improved phase stability of formamidinium lead triiodide perovskite by strain relaxation. *ACS Energy Lett.* **1**, 1014–1020 (2016).
28. Syzgantseva, O. A., Saliba, M., Gratzel, M. & Rothlisberger, U. Stabilization of the perovskite phase of formamidinium lead triiodide by methylammonium, Cs, and/or Rb doping. *J. Phys. Chem. Lett.* **8**, 1191–1196 (2017).
29. Yi, C. et al. Entropic stabilization of mixed A-cation ABX_3 metal halide perovskites for high performance perovskite solar cells. *Energy Environ. Sci.* **9**, 656–662 (2016).
30. Jong, U.-G., Yu, C.-J., Ri, J.-S., Kim, N.-H. & Ri, G.-C. Influence of halide composition on the structural, electronic, and optical properties of mixed $CH_3NH_3Pb(I_{1-x}Br_x)_3$ perovskites calculated using the virtual crystal approximation method. *Phys. Rev. B* **94**, 125139 (2016).
31. Jong, U.-G. et al. Revealing the stability and efficiency enhancement in mixed halide perovskites $MAPb(I_{1-x}Cl_x)_3$ with ab initio calculations. *J. Power Sources* **350**, 65–72 (2017).
32. Han, Y. et al. Degradation observations of encapsulated planar $CH_3NH_3PbI_3$ perovskite solar cells at high temperatures and humidity. *J. Mater. Chem. A* **3**, 8139–8147 (2015).
33. Leijtens, T. et al. Towards enabling stable lead halide perovskite solar cells; interplay between structural, environmental, and thermal stability. *J. Mater. Chem. A* **5**, 11483–11500 (2017).
34. Buin, A. et al. Materials processing routes to trap-free halide perovskites. *Nano Lett.* **14**, 6281–6286 (2014).
35. Aschauer, U., Pfenninger, R., Selbach, S. M., Grande, T. & Spaldin, N. A. Strain-controlled oxygen vacancy formation and ordering in $CaMnO_3$. *Phys. Rev. B* **88**, 54111 (2013).
36. Liu, Y. et al. Atomistic origins of surface defects in $CH_3NH_3PbBr_3$ perovskite and their electronic structures. *ACS Nano* **11**, 2060–2065 (2017).
37. Aristidou, N. et al. Fast oxygen diffusion and iodide defects mediate oxygen-induced degradation of perovskite solar cells. *Nat. Commun.* **8**, 15218 (2017).
38. Aristidou, N. et al. The role of oxygen in the degradation of methylammonium lead trihalide perovskite photoactive layers. *Angew. Chem. Int. Ed.* **54**, 8208–8212 (2015).
39. Lu, Y. et al. Effective calcium doping at the B-site of $BaFeO_{3-\delta}$ perovskite: towards low-cost and high-performance oxygen permeation membranes. *J. Mater. Chem. A* **5**, 7999–8009 (2017).
40. Stranks, S. D. et al. Electron–hole diffusion lengths exceeding 1 micrometer in an organometal trihalide perovskite absorber. *Science* **342**, 341–344 (2013).
41. Lee, M. M., Teuscher, J. J., Miyasaka, T., Murakami, T. N. & Snaith, H. J. Efficient hybrid solar cells based on meso-superstructured organometal halide perovskites. *Science* **338**, 643–647 (2012).
42. Dar, M. I. et al. Investigation regarding the role of chloride in organic–inorganic halide perovskites obtained from chloride containing precursors. *Nano Lett.* **14**, 6991–6996 (2014).
43. Colella, S. et al. Elusive presence of chloride in mixed halide perovskite solar cells. *J. Phys. Chem. Lett.* **5**, 3532–3538 (2014).
44. Chen, Q. et al. The optoelectronic role of chlorine in $CH_3NH_3PbI_3(Cl)$-based perovskite solar cells. *Nat. Commun.* **6**, 7269 (2015).
45. Starr, D. E. et al. Direct observation of an inhomogeneous chlorine distribution in $CH_3NH_3PbI_{3-x}Cl_x$ layers: surface depletion and interface enrichment. *Energy Environ. Sci.* **8**, 1609–1615 (2015).
46. Yin, W.-J., Chen, H., Shi, T., Wei, S.-H. & Yan, Y. Origin of high electronic quality in structurally disordered $CH_3NH_3PbI_3$ and the passivation effect of Cl and O at grain boundaries. *Adv. Electron. Mater.* **1**, 1500044 (2015).
47. Fan, L. et al. Elucidating the role of chlorine in perovskite solar cells. *J. Mater. Chem. A* **5**, 7423–7432 (2017).
48. Liao, H.-C. et al. Enhanced efficiency of hot-cast large-area planar perovskite solar cells/modules having controlled chloride incorporation. *Adv. Energy Mater.* **7**, 1601660 (2017).
49. Wu, X. et al. Trap states in lead iodide perovskites. *J. Am. Chem. Soc.* **137**, 2089–2096 (2015).
50. Jung, Y.-K., Lee, J.-H., Walsh, A. & Soon, A. Influence of Rb/Cs cation-exchange on inorganic Sn halide perovskites: from chemical structure to physical properties. *Chem. Mater.* **29**, 3181–3188 (2017).
51. Walsh, A., Scanlon, D. O., Chen, S., Gong, X. G. & Wei, S.-H. Self-regulation mechanism for charged point defects in hybrid halide perovskites. *Angew. Chem. Int. Ed* **54**, 1791–1794 (2015).
52. Noh, J. H., Im, S. H., Heo, J. H., Mandal, T. N. & Seok, S.II Chemical management for colorful, efficient, and stable inorganic-organic hybrid nanostructured solar cells. *Nano Lett.* **13**, 1764–1769 (2013).
53. Dastidar, S. et al. High chloride doping levels stabilize the perovskite phase of cesium lead iodide. *Nano Lett.* **16**, 3563–3570 (2016).
54. Dunlap-Shohl, W. A., Younts, R., Gautam, B., Gundogdu, K. & Mitzi, D. B. Effects of Cd diffusion and doping in high-performance perovskite solar cells using CdS as electron transport layer. *J. Phys. Chem. C* **120**, 16437–16445 (2016).

55. Kubicki, D. J. et al. Phase segregation in Cs-, Rb- and K-doped mixed-cation $(MA)_x(FA)_{1-x}PbI_3$ hybrid perovskites from solid-state NMR. *J. Am. Chem. Soc.* **139**, 14173–14180 (2017).
56. Domanski, K., Alharbi, E. A., Hagfeldt, A., Grätzel, M. & Tress, W. Systematic investigation of the impact of operation conditions on the degradation behaviour of perovskite solar cells. *Nat. Energy* **3**, 61–67 (2018).
57. Barker, A. J. et al. Defect-assisted photoinduced halide segregation in mixed-halide perovskite thin films. *ACS Energy Lett.* **2**, 1416–1424 (2017).
58. Saidaminov, M. I. et al. High-quality bulk hybrid perovskite single crystals within minutes by inverse temperature crystallization. *Nat. Commun.* **6**, 7586 (2015).
59. Kadro, J. M., Nonomura, K., Gachet, D., Grätzel, M. & Hagfeldt, A. Facile route to freestanding $CH_3NH_3PbI_3$ crystals using inverse solubility. *Sci. Rep.* **5**, 11654 (2015).
60. Liu, Y. et al. Two-inch-sized perovskite $CH_3NH_3PbX_3$ (X = Cl, Br, I) crystals: growth and characterization. *Adv. Mater.* **27**, 5176–5183 (2015).
61. Zhang, T. et al. A facile solvothermal growth of single crystal mixed halide perovskite $CH_3NH_3Pb(Br_{1-x}Cl_x)_3$. *Chem. Commun.* **51**, 7820–7823 (2015).
62. Nazarenko, O., Yakunin, S., Morad, V., Cherniukh, I. & Kovalenko, M. V. Single crystals of caesium formamidinium lead halide perovskites: solution growth and gamma dosimetry. *NPG Asia Mater.* **9**, e373 (2017).
63. Park, N.-G., Grätzel, M., Miyasaka, T., Zhu, K. & Emery, K. Towards stable and commercially available perovskite solar cells. *Nat. Energy* **1**, 16152 (2016).
64. Quan, L. N. et al. Ligand-stabilized reduced-dimensionality perovskites. *J. Am. Chem. Soc.* **138**, 2649–2655 (2016).
65. Perdew, J. P., Burke, K. & Ernzerhof, M. Generalized gradient approximation made simple. *Phys. Rev. Lett.* **77**, 3865–3868 (1996).
66. VandeVondele, J. & Hutter, J. Gaussian basis sets for accurate calculations on molecular systems in gas and condensed phases. *J. Chem. Phys.* **127**, 114105 (2007).
67. Press, W. H. *Numerical Recipes: The Art of Scientific Computing* (Cambridge Univ. Press, Cambridge, 2007).

Acknowledgements

This publication is partly based on work supported by an award (KUS-11-009-21) from the King Abdullah University of Science and Technology, by the Ontario Research Fund and by the Natural Sciences and Engineering Research Council of Canada. M.I.S. acknowledges the support of the Banting Postdoctoral Fellowship Program, administered by the Government of Canada. The work of A. Jain is supported by the IBM Canada Research and Development Center through the Southern Ontario Smart Computing Innovation Platform (SOSCIP) postdoctoral fellowship. DFT calculations were performed on the IBM BlueGene Q supercomputer with support from the SOSCIP. H.T. acknowledges the Netherlands Organization for Scientific Research (NWO) for a Rubicon grant (680-50-1511) in support of his postdoctoral research at the University of Toronto. We thank R. Wolowiec, D. Kopilovic, L. Levina and E. Palmiano for their help during the course of the study.

Author contributions

M.I.S. and J.K. conceived the idea, grew crystals, fabricated all devices and characterized them. A. Jain and O.V. performed DFT calculations. A. Johnston assisted in PL measurements. H.T. and F.T. assisted in solar cell fabrication and testing. R.Q.B. performed XPS. G.L., Y.Z. and H.T. assisted with the experiments and discussions. O.V. and E.H.S directed the overall research. M.I.S., J.K., O.V. and E.H.S. wrote the manuscript. All authors read and commented on the manuscript.

Competing interests

The authors declare no competing interests.

Additional information

Supplementary information is available for this paper at https://doi.org/10.1038/s41560-018-0192-2.

Reprints and permissions information is available at www.nature.com/reprints.

Correspondence and requests for materials should be addressed to E.H.S.

Publisher's note: Springer Nature remains neutral with regard to jurisdictional claims in published maps and institutional affiliations.

nature research

Corresponding author(s): Edward H. Sargent

Solar Cells Reporting Summary

Nature Research wishes to improve the reproducibility of the work that we publish. This form is intended for publication with all accepted papers reporting the characterization of photovoltaic devices and provides structure for consistency and transparency in reporting. Some list items might not apply to an individual manuscript, but all fields must be completed for clarity.

For further information on Nature Research policies, including our data availability policy, see Authors & Referees.

Experimental design

Please check: are the following details reported in the manuscript?

1. Dimensions			
Area of the tested solar cells	☒ Yes ☐ No	The area of solar cells is 0.049 cm2 (Methods, Solar cell characterization)
Method used to determine the device area	☒ Yes ☐ No	The active area was determined by the aperture shade mask (Methods, Solar cell characterization)
2. Current-voltage characterization			
Current density-voltage (J-V) plots in both forward and backward direction	☒ Yes ☐ No	Supplementary Table 6 and Supplementary Figure 17
Voltage scan conditions *For instance: scan direction, speed, dwell times*	☒ Yes ☐ No	JV curves were measured with a scanning rate of 50 mV/s (voltage step of 10 mV and delay time of 200 ms) (Methods, Solar cell characterization)
Test environment *For instance: characterization temperature, in air or in glove box*	☒ Yes ☐ No	Performance measurements were carried in both nitrogen and air ambient environments (Main text and Methods, Solar cell characterization)
Protocol for preconditioning of the device before its characterization	☒ Yes ☐ No	No preconditioning was used
Stability of the J-V characteristic *Verified with time evolution of the maximum power point or with the photocurrent at maximum power point; see ref. 7 for details.*	☒ Yes ☐ No	Maximum power point measurements were conducted (Figure 5c, d)
3. Hysteresis or any other unusual behaviour			
Description of the unusual behaviour observed during the characterization	☒ Yes ☐ No	Engineered solar cells showed negligible hysteresis
Related experimental data	☒ Yes ☐ No	Supplementary Table 6 and Supplementary Figure 17
4. Efficiency			
External quantum efficiency (EQE) or incident photons to current efficiency (IPCE)	☒ Yes ☐ No	Supplementary Figure 14b
A comparison between the integrated response under the standard reference spectrum and the response measure under the simulator	☒ Yes ☐ No	The integrated Jsc from EQE spectra is consistent with the Jsc from JV measurements (Supplementary Figure 14)
For tandem solar cells, the bias illumination and bias voltage used for each subcell	☐ Yes ☒ No	No tandem cells reported in this manuscript
5. Calibration			
Light source and reference cell or sensor used for the characterization	☒ Yes ☐ No	Newport, Class A simulator is used for the measurements (Methods, Solar Cell characterization)
Confirmation that the reference cell was calibrated and certified	☒ Yes ☐ No	The light intensity was calibrated by reference solar cell by Newport

Calculation of spectral mismatch between the reference cell and the devices under test	☒ Yes ☐ No	Mismatch factor of 1 was used in our measurements

6. Mask/aperture

Size of the mask/aperture used during testing	☒ Yes ☐ No	0.049 cm2 (Methods, Solar Cell characterization)
Variation of the measured short-circuit current density with the mask/aperture area	☐ Yes ☒ No	We haven't measure the cells with apertures of different sizes

7. Performance certification

Identity of the independent certification laboratory that confirmed the photovoltaic performance	☐ Yes ☒ No	We did not certify our cells. But CsMAFA control devices were certified and reported in our previous paper (Science 2017, 355, 722)
A copy of any certificate(s) *Provide in Supplementary Information*	☐ Yes ☒ No	We did not certify our cells

8. Statistics

Number of solar cells tested	☒ Yes ☐ No	At least 30 devices for each composition were tested (Figure 5a and Supplementary Figure 13)
Statistical analysis of the device performance	☒ Yes ☐ No	Figure 5a and Supplementary Figure 13

9. Long-term stability analysis

Type of analysis, bias conditions and environmental conditions *For instance: illumination type, temperature, atmosphere humidity, encapsulation method, preconditioning temperature*	☒ Yes ☐ No	The stability test at MPP operation conditions under AM 1.5G simulated illumination with a 420-nm cutoff UV-filter was carried out in both nitrogen and ambient air for unencapsulated solar cells (Methods, Solar cell characterization)